pubs.acs.org/Biomac

Article

Charge-Symmetry-Mediated Liquid–Liquid Phase Separation Enables Tailored High-Protein Food Models

Jiaxuan Zhang, Jiajia Zhou, Fei Pan, Jiabao Zheng,* and Weizheng Sun*

Cite This: https://doi.org/10.1021/acs.biomac.6c00197

Read Online

ABSTRACT: Precise control of the matter state and dynamics is a key challenge in developing novel food matrices using concentrated protein coacervates. Herein, we report a pH-driven liquid–gel–solid transition of protein coacervates composed of β-lactoglobulin (BLG) and lysozyme (LYS). The terminal relaxation time of the coacervate extended from 0.17 ms to 267 s during the phase transition due to increased affinity. Spin–spin relaxation data, hydrogen bond competition experiments, and molecular dynamics simulations revealed that increasing the pH from 6 to 8 shifted the BLG/LYS stoichiometric ratio from 3:1 to 1:1. The enhanced charge symmetry expanded the interaction interface between BLG and LYS by 1.8 times, thereby promoting the desolvation of bound water and the formation of protein–protein hydrogen bonds that consequently slowed the dynamics of the BLG-LYS coacervates. Overall, this study introduces a new class of protein-based food models with tunable physical properties and offers valuable insights into their precise control.

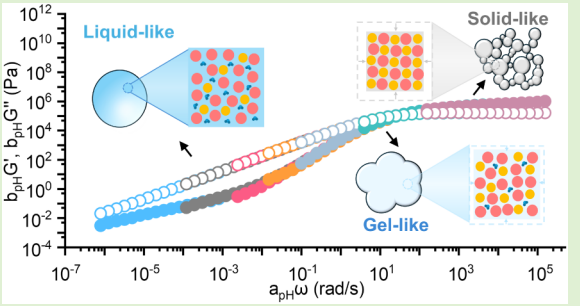

1. INTRODUCTION

Complex coacervation is a liquid–liquid phase separation (LLPS) phenomenon driven by multivalent interactions between biomacromolecules and synthetic polymers. The enthalpy gain overcomes the entropy of mixing, leading to two coexisting phases: a low-concentration dilute phase and a high-concentration coacervate phase.[1,2] Over the past decade, LLPS of proteins and nucleic acids within cells has been shown to drive the formation of membrane-less organelles and biomolecular condensates, significantly advancing coacervation science.[3] Intrinsically disordered proteins (IDPs) and hybrid proteins with IDP regions (IDPRs) facilitate biological LLPS due to their repetitive amino acid sequences, highly flexible chains, dynamically heterogeneous conformations, and ability to form multivalent and transient intermolecular interactions.[2,4] However, most food proteins, including soy proteins (e.g., glycinin, β-conglycinin), whey proteins (e.g., β-lactoglobulin, α-lactalbumin), pea proteins (e.g., vicilin, legumin), and egg proteins (e.g., ovalbumin, lysozyme), are structured proteins with stable tertiary structures. Given their few charged residues, reduced conformational flexibility, and low surface charge anisotropy,[5] food proteins would seem unlikely candidates for LLPS. However, recent studies have established that they can readily undergo LLPS, forming heteroprotein complex coacervates (HPCCs). The phase separation is driven by the multiple modular interaction domains,[6,7] as seen in combinations such as β-conglycinin/lysozyme,[8,9] β-lactoglobulin/lactoferrin,[10−15] and pea protein isolate/lactoferrin.[16] These findings open a new avenue for designing novel protein-based soft food matrices using protein assembly and phase transition in food applications.

Although coacervates have long been recognized as having a liquid nature since Bungenberg de Jong and Kruyt[3,17,18] discovered them, and their connection with modern cellular architectures and protocells was established by Anthony Hyman and Clifford Brangwynne,[19] recent discoveries of diverse biomolecular condensates have shown that systems undergoing LLPS can evolve into a variety of physical states, including liquids, gels, and solids.[3,17,18] The physical state of biomolecular condensates is closely tied to their function. For example, highly dynamic, liquid-like condensates (e.g., stress granules,[20,21] P granules,[19] nucleoli[1]) can rapidly adapt to environmental changes through structural rearrangement, thereby facilitating essential chemical reactions such as ribosome biogenesis, mRNA translation regulation, and specific enzymatic cascades. In addition to restricting macromolecular diffusion, gel-like condensates (e.g., centrosomes,[22] RNA expansion repeats,[23] nuclear pores[24]) perform key mechanical functions, including the generation of mechanical forces and resistance to external stress. Solid condensates (e.g., Balbiani body,[25] A-bodies[26]) can isolate molecules and halt

Received: January 28, 2026
Revised: April 19, 2026
Accepted: April 22, 2026

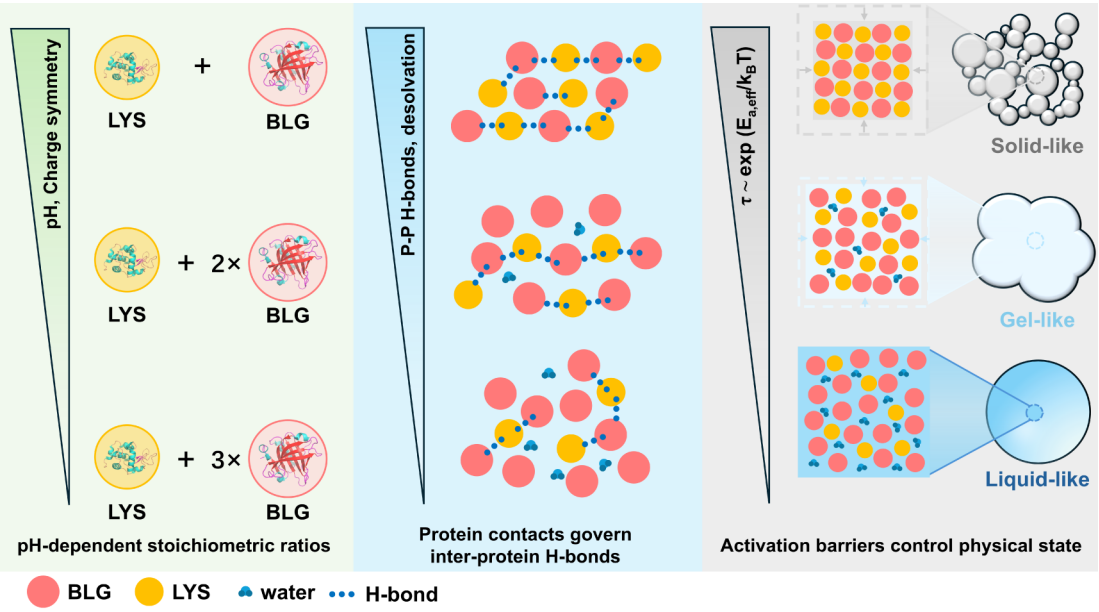

Figure 1. Schematic diagram of charge-symmetry-induced liquid−gel−solid transition of coacervates across multiple spatial scales.

biochemical reactions, thereby providing protection against environmental or mechanical stress. However, sequence mutations and microenvironment alterations can alter condensate physical properties, often associated with functional loss, abnormal physiological responses, and neurodegenerative diseases.[3,18,27] Recent studies on the relaxation dynamics of synthetic and natural polyelectrolyte complexes (PECs) have clarified how molecular parameters (e.g., chirality,[28−30] charge pattern,[31−36] hydrophobicity,[37−42] chain length[43−47]) and environmental conditions (e.g., salt ions,[45,48−50] temperature,[47,51−53] pH[54,55]) govern the physical properties. These insights are critical for applications in 3D bioprinting and electrospinning.[56−62]

We want to explore the exquisite interactions and thermodynamics between heterologous food proteins to create protein-based soft matter with desirable physical properties. Such materials can spontaneously assemble, thus avoiding complex processing or expensive equipment. Unlike membranized artificial cells and intracellular condensates that require dynamic biochemical regulation, coacervate droplets self-assemble in vitro and coalesce under interfacial tension into a dense, processable phase.[63,64] In classical polymer theory, LLPS occurs when the protein concentration surpasses the solubility limit or critical concentration threshold. The abrupt enrichment in protein volume fraction makes coacervates far exceed the protein content of typical colloidal assemblies (e.g., colloidal gels, fibrillar gels, and emulsions) derived from protein solutions.[65] Therefore, food protein coacervates represent a distinct class of highly crowded soft matter systems that are fundamentally distinct from conventional protein solutions, offering significant potential for engineering innovative protein-based food systems. Although extensive research has elucidated coacervation mechanisms of synthetic polyelectrolytes and disordered biomolecules, the mechanistic insight into coacervates composed exclusively of globular proteins, particularly their phase behavior, physical states, and emergent material properties, remains inadequately characterized. Bridging this knowledge gap is not only a key scientific challenge but also a pathway to designing next-generation high-protein food substrates and nutritional supplements with tunable material properties.

In this study, we investigated the LLPS-driven coacervates formed by oppositely charged β-lactoglobulin (BLG) and lysozyme (LYS). By modulating pH-dependent charge symmetry to regulate protein−protein hydrogen bonding and desolvation, we demonstrated a platform for creating food-protein-based materials with widely tunable physical properties. BLG, a major whey-derived byproduct of dairy processing, and LYS, sourced from egg whites, are both widely used in food applications and have well-documented safety profiles.[66] Their well-defined globular structures make them ideal model systems for investigating soft matter behavior and protein physics in food science. To elucidate the pH-driven liquid−gel−solid transition of BLG-LYS HPCCs, we analyzed coacervate relaxation properties across nine decades in frequency space using time-pH superposition and examined water dynamics within the coacervate phase (Figure 1). We also quantified the thermodynamic parameters of protein interactions and desolvation during LLPS to uncover the thermodynamics behind pH-dependent transitions in physical states. The role of protein−protein hydrogen bonding and desolvation in phase transitions was confirmed by urea-induced inversion of both phase state and dynamics. Furthermore, all-atom molecular dynamics (MD) simulations and coarse-grained (CG) simulations provided molecular-level insights that validated and complemented the experimental findings. Finally, the high protein content and customizable physical properties of HPCCs demonstrate their potential as next-generation high-protein food substrates and nutritional supplements.

2. EXPERIMENTAL SECTION

2.1. Materials

The LYS powder (62971, ~70000 U/mg, from chicken egg white) was purchased from Sigma-Aldrich (St. Louis, USA). The BLG powder (L304933, protein ≥ 95%, derived from milk) was purchased from Aladdin Biochemical Technology Co., Ltd. (Shanghai, China). Inductively coupled plasma optical emission spectrometry showed

https://doi.org/10.1021/acs.biomac.6c00197
Biomacromolecules XXXX, XXX, XXX−XXX

that BLG contained 1.020% K, 0.740% Na, 0.076% Ca, and 0.014% Mg. LYS contained 0.100% Na, 0.073% Ca, 0.023% K, and 0.079% Mg. The bicinchoninic acid (BCA) kit was purchased from Guangzhou Dingguo Biotechnology Co., Ltd. (Beijing, China). NaH_2PO_4, HCl, NaOH, and urea were purchased from Sinopharm Chemical Reagent Co., Ltd. (Shanghai, China). Milli-Q water (18.2 MΩ·cm) was used for all experiments (Millipore Corp., Bedford, MA).

2.2. Preparation of BLG-LYS Coacervates

BLG and LYS solutions (5 mg/mL) were prepared by dissolving the protein powders in Milli-Q water and magnetically stirring at 450 rpm for 6 h to fully hydrate. The stock solutions were filtered through 0.22 μm syringe filters to remove the residues. For urea-containing coacervates, urea was added after filtration. The stock solutions were adjusted to their target pH using 0.1 M NaOH or HCl and then mixed in a series of mass ratios. The mixture was then centrifuged (8000 × g, 20 min) to obtain the coacervate phase, which was then stored 6 h to allow for equilibration and used in subsequent measurements except ζ-potential, turbidity, and isothermal titration calorimetry measurements. All experiments were conducted at 25 °C.

2.3. ζ-Potential Measurements

The ζ-potential of the protein solutions and mixtures was determined by a Malvern Zetasizer Nano ZS. The samples were loaded into disposable electrophoretic mobility cells (DTS1070, Malvern, United Kingdom) and equilibrated for 120 s. The dielectric constant and the refractive index of the solvent were set at 78.5 and 1.333, respectively.

2.4. Turbidity Measurements

Turbidity measurements were conducted at 600 nm using 1 cm path length glass cuvettes using a SHIMADZU UV-1800 spectrophotometer (SHIMADZU Co., Japan), with Milli-Q water serving as a reference for 100% transmittance (T). The turbidity was quantified as follows (eq 1):

$$\text{Turbidity} = -\ln T \tag{1}$$

2.5. Protein Recovery Ratio

Protein recovery of BLG-LYS complex coacervates was quantified using the BCA assay with bovine albumin as the standard reference protein. The recovery ratio was calculated by subtracting the supernatant protein concentration after phase separation from the initial protein concentration before phase separation. The supernatant was obtained by centrifuging the BLG-LYS mixture at 8000 × g for 20 min and then diluted 4-fold with Milli-Q water to achieve an appropriate concentration for analysis.

2.6. Optical Microscopy Observation

The morphology of BLG-LYS coacervates was observed by bright-field microscopy (Mshot MF31, Guangzhou, China) with a 40× magnification objective.

2.7. Scanning Electron Microscopy (SEM)

The microstructure of the freeze-dried BLG-LYS coacervates was scanned with SEM (SU8600 Hitachi, Tokyo, Japan) at an accelerating voltage of 5.0 kV and a magnification of 5000×. The coacervate powder, obtained through freeze-drying (Alpha 1−4 LD, Christ Company, Germany), was mounted on aluminum stubs using double-sided carbon tape and coated with a thin gold film by using a sputter coater for surface morphology scanning.

2.8. Small-Angle X-ray Scattering (SAXS)

The BLG-LYS coacervates were placed in 304 stainless steel flat washers (inner diameter D, outer diameter D_C, thickness 5 mm, 9 mm, and 0.8 mm, respectively) and sealed with polyimide tape. Small-angle X-ray scattering (SAXS) measurements were performed using a small-angle X-ray scatterometer (Xeuss 2.0, Xenocs, France), with a wavelength of λ = 1.34 Å and an X-ray source of MetalJet-D2 (Excillum, Switzerland). The detector used was a two-dimensional Pilatus3R 1 M (Dectris, Switzerland) with pixel sizes of PSize1 = 0.000172 m and PSize2 = 0.000172 m, positioned 2.52 m from the sample, with an exposure time of 1800 s. The scattering wave vector Q ranged from 0.005 to 0.25 $Å^{-1}$, corresponding to observable length scales between 2.5 and 125.7 nm in real space.

2.9. Linear Viscoelasticity Measurements

The linear viscoelasticity of the BLG-LYS coacervates was determined by using small-amplitude oscillatory shear measurements on an Anton Paar MCR702e strain-controlled instrument (Anton Paar GmbH, Austria). Strain amplitude measurements ranging from 0.1% to 10% at 100 rad/s were conducted to determine the linear viscoelastic region (Figure S3a,b). Frequency sweeps were then conducted from 100 to 0.1 rad/s at a fixed strain of 0.1% within the linear viscoelastic regime, using a 25 mm diameter measuring cone with a 1° angle (CP25−1) and a gap value of 0.5 mm as well as a 25 mm diameter measuring plate (PP25) with a gap value of 1 mm. Two milliliters of supernatant were poured around the geometry to prevent evaporation. The temperature was maintained at 25 °C by using a Peltier cell connected to a recirculating bath, and all measurements were performed with a normal force below 0.1 N to ensure fully relaxed systems.

2.10. Time-pH Superposition

Time-pH superposition and time-pH-urea superposition were determined according to the method of Es Sayed et al.,[37] with minor modifications. Prior to conducting the superposition, the plot of the loss factor, tan δ, as a function of the angular frequency, ω, was generated to qualitatively assess the feasibility of time-pH superposition and time-pH-urea superposition for a series of coacervates as a function of pH and urea concentration. The horizontal shift factors, denoted as a_{pH} and $a_{pH\text{-}urea}$, were determined from the plot of tan δ as a function of ω, taking the data from the sample prepared at pH 7.0 (0 M urea) as the reference. Correspondingly, the vertical shift factors, b_{pH} and $b_{pH\text{-}urea}$, were obtained by vertically shifting the viscoelastic curves to match those of G' and G''.

2.11. Isothermal Titration Calorimetry (ITC)

The ITC experiment was conducted using a Microcal PEAQ-ITC (Malvern Panalytical Ltd., UK) according to the method described by Zheng et al.[6] with minor modifications. BLG solution (1 mg/mL) and LYS solution (5, 10, and 14 mg/mL) at varying pH levels (6.0, 7.0, and 8.0) were prepared following the protocol described in Section 2.2, using 5 mM sodium phosphate buffer in place of deionized water. Apparent thermodynamic parameters including the binding constant (K_{app}), enthalpy change (ΔH_{app}), entropy change ($-T\Delta S_{app}$), and binding stoichiometry (N) were calculated by iterative curve fitting of the binding isotherms. The "One Set of Sites" binding model, provided with Microcal software, was employed to fit the binding isotherms. The Gibbs free energy (ΔG_{app}) was calculated as follows (eq 2):

$$\Delta G_{app} = -RT\ln K_{app} \tag{2}$$

2.12. Water Content and Dynamics Analysis

The total water content of the coacervates was determined using a METTLER TOLEDO TGA 2 (Mettler Toledo, Switzerland). Around 10 to 20 mg of the sample was placed in a crucible. Then, the crucible was transferred to a furnace and heated to 150 °C at a rate of 20 °C/min and held isothermally for 8 min to ensure complete dehydration. Subsequently, the temperature was increased to 700 °C at a rate of 20 °C/min to completely combust the organic matter. The heating and holding stages were conducted under a nitrogen atmosphere (20 mL/min), while the final heating stage utilized oxygen (20 mL/min). The mass fractions of the protein were calculated by recording the mass loss during the final heating process. Since the coacervates experienced slight mass loss between weighing and the start of the analysis, the mass fractions of water were obtained by subtracting the protein mass from the total mass.

The relaxation state of water in the coacervate was analyzed using low-field nuclear magnetic resonance spectroscopy with the NMI 20−040H−I (Niumag Analytical Instrument Co., Ltd., Suzhou, China) under a magnetic field of 0.50 ± 0.05 T and a proton resonance frequency of 21 MHz. Approximately 1 g of the sample was placed in

https://doi.org/10.1021/acs.biomac.6c00197
Biomacromolecules XXXX, XXX, XXX−XXX

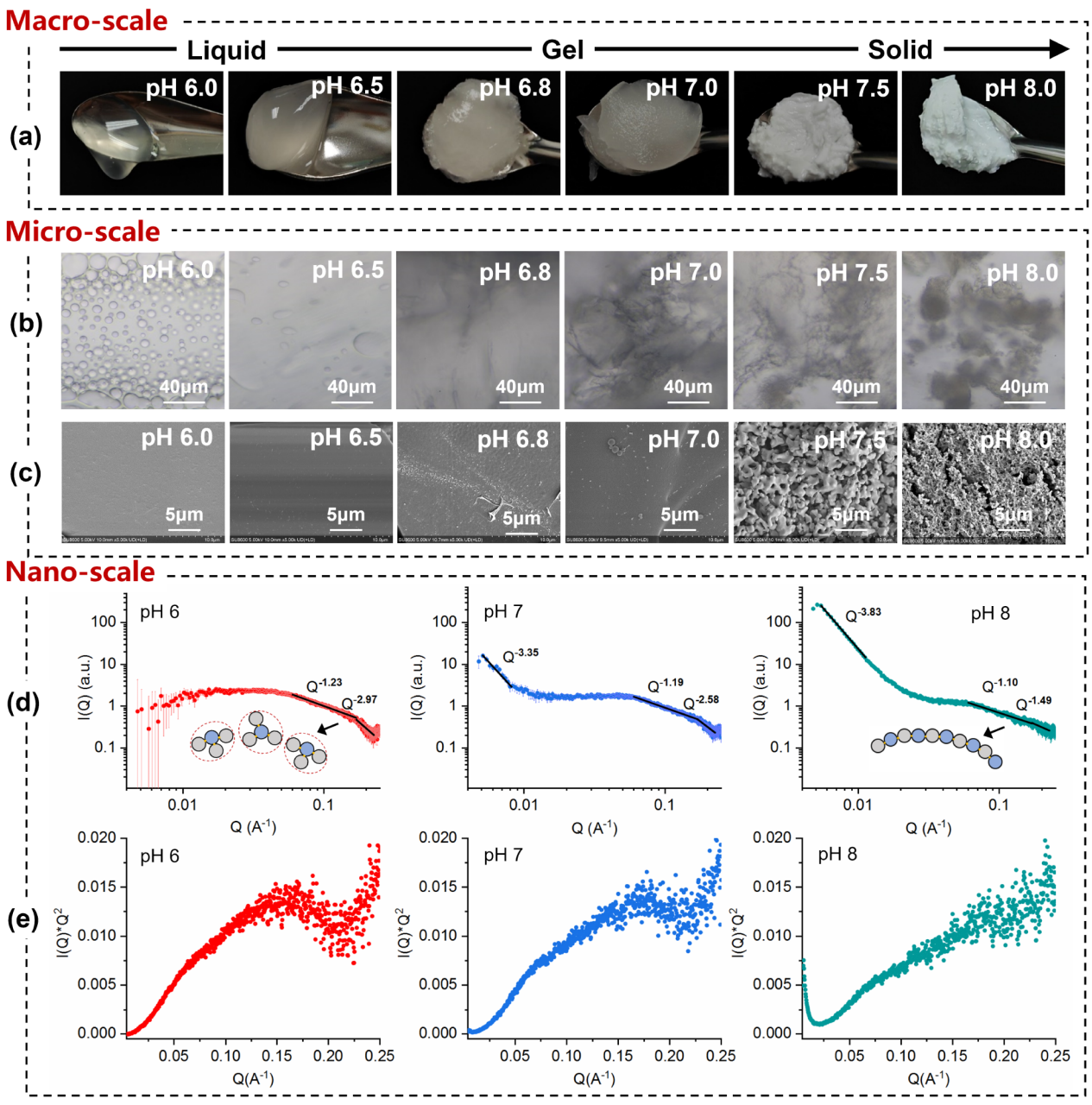

Figure 2. Images of BLG-LYS coacervates at pH 6−8 across multiple spatial scales: macroscopic photos (a), bright-field microscopy images (b), scanning electron microscopy images (c), background-subtracted scattering intensity $I(Q)$ as a function of wave vector Q (d), and Kratky plots (e).

a 40 mm NMR sample tube for measurement. The transverse relaxation time (T_2) was determined using a Carr−Purcell−Meiboom−Gill (CPMG) pulse sequence at 32 °C, with a waiting time of 10000 ms, an echo time of 0.200 ms, 8000 echoes, and 4 repeat scans. The CPMG decay curve was analyzed by exponential fitting using the instrument's inversion software, Niumag MultiExp Inv Analysis, with 10000 inversion iterations. From the fitting, the intrinsic T_2 peak position, peak area (A_2), and relative percentage of each peak (%) were calculated.

2.13. Fourier Transform Infrared Spectroscopy (FTIR)

Fourier transform infrared (FTIR) spectroscopy of BLG, LYS, and BLG-LYS coacervates was conducted using a Nicolet iS50-Nicolet Continuum instrument (Thermo Fisher Scientific Inc., USA). Spectra of freeze-dried samples were collected with an average of 32 scans over a wavenumber range of 4000−400 cm^{-1} at a resolution of 4 cm^{-1}. The background spectra were acquired under conditions identical to those of the sample measurements. Peak positions were identified by using the automatic peak-finding algorithm available in Origin 2021.

2.14. All-Atom Molecular Dynamics Simulation

The crystal structures of BLG and LYS were obtained from the RCSB database, with the codes 3NPO and 1DPX, respectively. Missing residues were repaired using the Swiss PDB Viewer tool,[67] and the protonation states of the structures at pH 6 and 8 were determined based on the H++ tool.[68] Molecular dynamics simulations were performed using GROMACS 2021.6 software.[69] The protein topology information was generated based on the Amber14sb force field. The insert-molecules tool was employed to construct simulation systems at pH 6 and 8 with protein ratios of 3:1 and 2:2, respectively. Each system was explicitly solvated and placed in a cubic box filled with TIP3P water molecules. Counterions were added to neutralize the total charge of the system and maintain electroneutrality. Energy minimization was performed in two stages: first, using the steepest descent method (10000 kJ/mol/nm), followed by conjugate gradient

https://doi.org/10.1021/acs.biomac.6c00197
Biomacromolecules XXXX, XXX, XXX−XXX

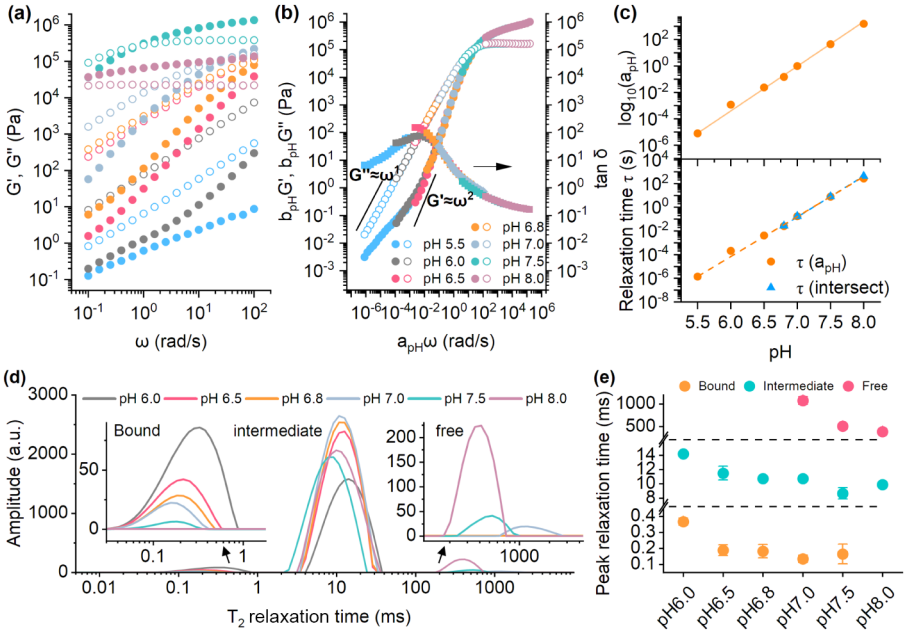

Figure 3. Frequency sweep data (a), time-pH superposition data with reference sample at pH 7.0 (b), horizontal shift factor (a_{pH}), and terminal relaxation time (τ) as a function of pH (c). T2 relaxation time (d), and peak relaxation times of bound, intermediate, and free water (e).

optimization (100.0 kJ/mol/nm). Subsequently, pre-equilibration of the system was carried out using the canonical ensemble (NVT, 1 ns) and the isothermal−isobaric ensemble (NPT, 1 ns) sequentially. All systems were simulated for 200 ns. Bonds involving hydrogen atoms were constrained by using the default Linear Constraint Solver (LINCS) algorithm. The V-rescale thermostat and the Parrinello-Rahman barostat were used to control the simulation temperature (298.15 K) and pressure (1.0 bar), with time constants of 0.1 and 2 ps, respectively. Long-range interactions were treated by using the Particle-Mesh Ewald (PME) method, with a cutoff of 10 Å for van der Waals interactions. A time step of 2 fs was employed, and snapshots were collected every 1 ps.

2.15. Coarse-Grained Molecular Dynamics Simulation

The coarse-grained (CG) models of BLG and LYS were constructed based on the Martini 3.0 guidelines provided on the Martini Web site. Their secondary structures were calculated using the DSSP program.[70] Simulation systems at pH 6 and 8 were built with protein ratios of 15:5 and 10:10, respectively. The LINCS algorithm was employed to constrain bond lengths within proteins as well as bonds between the backbone and side chains. All simulations began with energy minimization using the steepest descent integrator. Subsequently, a 40 ns temperature ramp-up MD simulation was performed under NVT conditions to stabilize the system at 298.15 K. This was followed by a 40 ns NPT simulation to equilibrate the system at a pressure of 1.0 bar. Finally, an unrestricted 2 μs MD simulation was conducted at 298.15 K. The solvent-accessible surface area (SASA) of BLG, LYS, and the BLG-LYS complex was calculated by using the SASA module in GROMACS. The difference between the total SASA of BLG and LYS and that of the BLG-LYS complex was evaluated to quantify changes in the contact area between BLG and LYS in coacervates.

2.16. Statistical Analysis

Statistical analysis was performed using Excel 2013 (Microsoft, Redmond, WA, USA) and SPSS 19.0 (IBM, Armonk, NY, USA). Significant differences were determined using Duncan's multiple range test in SPSS. A *P*-value of less than 0.05 was considered statistically significant.

3. RESULTS AND DISCUSSION

3.1. pH-Driven Liquid−Gel−Solid Phase Transitions of Coacervates

This study reported a distinct liquid−gel−solid phase transition of BLG-LYS coacervates as the pH increased from 6 to 8. All coacervates were prepared at their respective pH-dependent stoichiometric ratios (Figure S1). As the pH increased from 6 to 8, the BLG/LYS mass ratio changed from 4:1 to 1.3:1 (with the molar ratio changing from 3.2:1 to 1:1). These changes were mainly attributed to the increased ionization of the carboxyl groups of Glu, accompanied by the decreased ionization of the amino groups of Lys and N-terminal amino acids and the imidazole groups of His, with increasing pH (Figure S2). This regular phase transition of BLG-LYS coacervates was elucidated by structural characterization at different length scales. This systematic transition in physical properties allows us to uniformly refer to the assemblies as coacervates throughout this paper, rather than distinguishing between coacervates and precipitates to represent liquid and solid phases, respectively.

Specifically, at the macroscale, the coacervate phase obtained by centrifugation appeared as a transparent liquid with good fluidity at pH 6 (Figure 2a). At the microscale, under bright-field microscopy, mixing BLG and LYS at pH 6 resulted in the formation of transparent spherical droplets capable of fusion, a characteristic of liquid coacervates (Figure 2b). The coacervate phase after freeze-drying was observed using SEM, and the liquid coacervate showed uniformity at the microscale (Figure 2c). SAXS was employed to investigate the assembly structure of coacervates at the nanoscale. In this study, the experimental *Q*-range was from 0.005 Å^{-1} to 0.25 Å^{-1}, corresponding to a size range of 125−2.5 nm ($d \approx 2\pi/Q$) (Figure 2d). In the high-*Q* region of 0.17 Å^{-1} to 0.25 Å^{-1}, the scattering intensities of BLG-LYS coacervates at pH 6 decayed with a power law of $Q^{-2.97}$, indicating that the primary unit of the BLG-LYS coacervates resembled a surface-roughened, three-dimensional spherical scatterer (Figure 2d).[71−73] The Kratky plot showed a

https://doi.org/10.1021/acs.biomac.6c00197
Biomacromolecules XXXX, XXX, XXX−XXX

bell-shaped peak at 4 nm, indicating a compact three-dimensional spherical assembly, with the upward slope after the peak suggesting a rod-like or chain-like extended structure (Figure 2e).[74] In the middle-Q region, the scattering intensity decayed with a power law of $Q^{-1.23}$, and in the low-Q region, no significant scattering was observed, consistent with their large-scale structural uniformity observed in SEM images and transparent macroscopic appearance (Figure 2a,d).

As the pH increased, the fluidity and transparency decreased and a translucent gel was formed at pH 6.8−7.0 (Figure 2a). Under bright-field microscopy, the coacervates formed after mixing exhibited larger gel-like blocks (Figure 2b). SAXS analysis showed that in the high-Q region, the scattering intensity decayed with a power law of $Q^{-2.58}$, indicating surface roughness and certain mass fractal characteristics; in the middle-Q region, the decay was $Q^{-1.19}$, suggesting the formation of rod-like structures; in the low-Q region, the coacervates at pH 7 ($Q^{-3.35}$) showed a lower power-law decay than at pH 8 ($Q^{-3.83}$), suggesting a lower degree of aggregation (Figure 2d,e).

Further increasing the pH to 7.5−8.0 resulted in a white solid precipitate (Figure 2a). When the pH was further raised to 8.0, the coacervates appeared as amorphous complexes with a nonuniform structure, and SEM revealed inhomogeneous aggregates (Figure 2b,c). This heterogeneity typically arises from the stalled structural relaxation following kinetic trapping. SAXS analysis showed that in the high-Q region, the scattering intensity decayed with a power law of $Q^{-1.49}$, indicating rod-like scatterers; in the middle-Q region, the decay of $Q^{-1.10}$ suggested further assembly of rod-like structures; and in the low-Q region, the coacervates exhibited a high power-law decay of $Q^{-3.83}$, indicating the aggregation of these rod-like units into larger structures (Figure 2d). At this length scale, aggregates typically caused strong light scattering, thus explaining the complete opacity of the macroscale coacervate phase at pH 8 (Figure 2a,b). The SAXS results provided a good description of the structural features of the primary units, as well as the larger-scale structural heterogeneity due to kinetic trapping. The structure of the primary units in the high-Q region and rod-like structures in the medium-Q region were verified by all-atom MD simulations and coarse-grained simulations, respectively (Supplementary Movies 1−4).

3.2. Dynamics of Liquid, Gel, and Solid Coacervates

The linear viscoelasticity of the BLG-LYS coacervates was further analyzed to understand the relaxation dynamics behind the transition in pH-driven physical properties and structural differences. The storage modulus (G') and loss modulus (G'') increased with increasing pH, except at pH 8, which is generally associated with the hardening of the coacervates (Figure 3a).[45] The terminal relaxation time (τ) of the coacervates, which reflects the time scale of the lifetime of the protein−protein interactions within the coacervates, is determined from the crossover frequency between the G' and G'' curves. For folded proteins, these interactions are mediated by "stickers", namely the interacting patches on the protein surface.[75] From pH 5.5 to 6.8, the viscoelastic response was dominated by G'', with τ far below the relaxation time of 0.06 s corresponding to the frequency maximum tested, indicating that the coacervates relaxed rapidly and displayed liquid-like behavior due to the transient nature of intermolecular interactions. As the pH increased to 7.0 and 7.5, the appearance of a $G'-G''$ crossover revealed the onset of gel-like properties, where the system transitioned from viscous to elastic response as a percolated protein network formed. The longer relaxation times (τ = 0.17 and 8.1 s) reflected the increasing stability and lifetime of these interactions. In contrast, at pH 8.0, τ exceeded 60 s, and the response was arrested across the frequency range, suggesting that strong association and aggregation of proteins led to kinetically trapped, solid-like structures with minimal capacity for relaxation. It should be noted that the observed rheological state is inherently coupled to the accessible frequency range; thus, the apparent dominance of G' or G'' often stems from the experimental time scale rather than an absolute thermodynamic identity.[76] As shown in Figure 3b, although G' consistently exceeded G'' within the tested frequency range for the pH 8.0 sample, the tan δ still exhibited a slight frequency dependence over longer time scales. Furthermore, Figure S6 clearly reveals that the tan δ curves at different frequencies converged toward a potential intersection point (the critical liquid-to-solid transition point) located beyond pH 8.0. These observations indicated that, according to the Winter−Chambon theory, even the coacervate at pH 8.0 technically remained in a pregelation state on a sufficiently long time scale.[77] However, within the accessible experimental time scale, the pH 8.0 sample exhibited behavior characteristic of a viscoelastic solid. Therefore, to better characterize the relaxation behavior in this regime, we adopted the modulidominance approach, classifying the samples as "liquid-like", "gel-like", or "solid-like" based on their dominant viscoelastic properties.

The linear viscoelasticity of the coacervates at pH 7.0 was used as the reference condition, and the relaxation dynamics of BLG-LYS coacervates across nine decades in frequency space were explored using time-pH superposition because the linear viscoelasticity obtained from frequency sweeping only allows the exploration of the relaxational behavior of the coacervates over a limited time scale (Figure 3b). This superposition analysis has been frequently used in recent studies to quantify the dynamics of various polyelectrolyte complexes as functions of salt concentration, polymer chemistry, and pH, but it has rarely been applied to the analysis of globular protein coacervates.[41,44,45,47,55,76,77,78] Traditionally, van Gurp−Palmen (tan δ vs complex modulus G^*) and Cole−Cole plots (G'' vs G') are employed to assess the homogeneous nature of polymer melts and composites, with a semicircle shape implying the absence of any heterogeneity in the material.[33,37,42,45,47] Consequently, as shown in Figure S3f,g, we observe that the data of varying pH collapse on one another, implying the same relaxation modes for all pH conditions. The continuity of tan δ indicated the good quality of the superposition, and the turning of the tan δ curve may be related to the additional forces in the liquid−gel−solid transition (Figure 3b). The successful superposition demonstrated the similarity in the relaxational behavior of these coacervates.[45,46,79]

The "sticky diffusion" theory and nonentangled sticky Rouse model were used to understand the results of time-pH superposition, because the scaling relations of the terminal curves are close to $G' \sim \omega^2$ and $G'' \sim \omega$ at pH 6.0 and 6.5 (Figure 3c).[45,51,80] The local friction is believed to be caused by the interaction between the protein stickers.[35] The average lifetime of the stickers is governed by the activation energy barrier of the interactions;[76] thus, the relaxation dynamics of the coacervates exhibit an exponential dependence on the pH-

https://doi.org/10.1021/acs.biomac.6c00197
Biomacromolecules XXXX, XXX, XXX−XXX

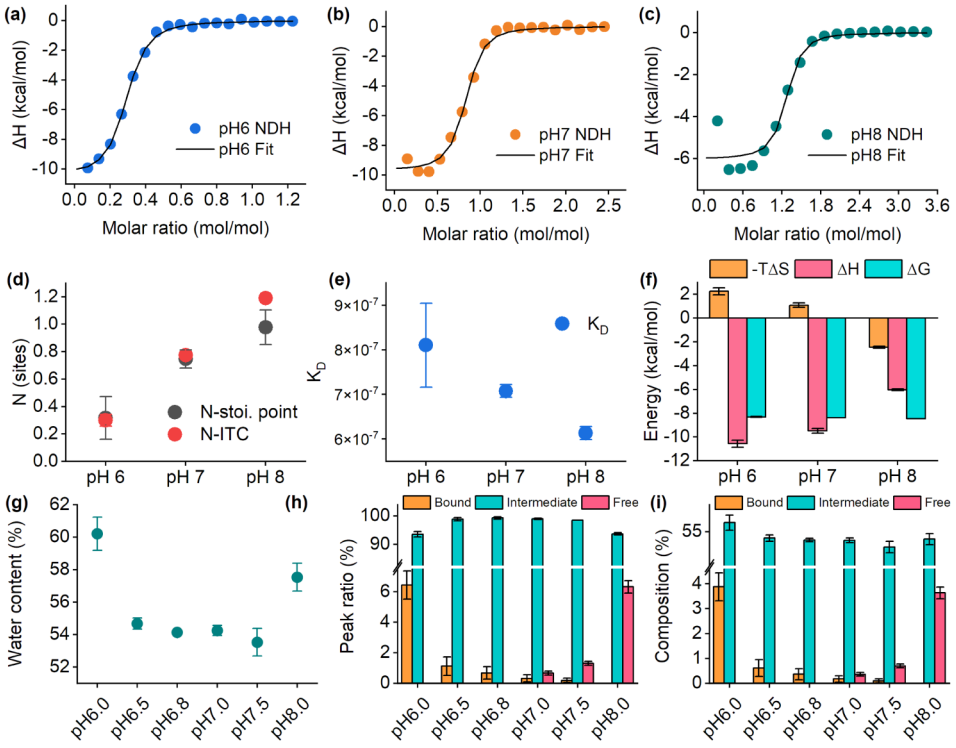

Figure 4. ITC titration graphs of BLG (1 mg/mL) with LYS (5, 10, and 14 mg/mL) at pH 6 (a), pH 7 (b), and pH 8 (c). ITC calorimetric data obtained from the fitting model of "one set of sites": binding site data (d), apparent dissociation constant $K_{d,app}$ (e), and changes in apparent entropy ($-T\Delta S_{app}$), apparent enthalpy (ΔH_{app}), and apparent total Gibbs free energy (ΔG_{app}) (f). Total water content of BLG-LYS coacervates (g). The ratio of the peak areas corresponding to bound, intermediate, and free water (h). The estimated contents of bound water, intermediate water, and free water were calculated by total water content and peak area ratio (i).

modulated energy levels. In this study, the power law of the shift factor a_{pH} showed a good linear relationship with pH (Figure 3c). Changing only one unit of pH affected the relaxation time by 3.4 orders of magnitude, suggesting that a decrease in pH significantly lowers the energy barrier for sticker dissociation, thereby accelerating the coacervate dynamics. The τ values of the liquid, gel, and solid coacervates at pH 6, 7, and 8 were 0.00017, 0.17, and 267 s, respectively, based on their shift factors a_{pH} and the τ of the coacervate at pH 7. This estimate was reasonable because it was consistent with the results obtained by the frequency crossover points. The corresponding vertical shift factors (b_{pH}) were presented as a function of pH in Figure S3c.

Low-field nuclear magnetic resonance (LF-NMR) and spin−spin relaxation techniques were also employed to investigate the relaxation dynamics of water in the BLG-LYS coacervates. As shown in Figure 3d, the relaxation times of strongly bound water and weakly bound water decreased significantly with increasing pH, indicating the slowdown of the bound water dynamics. The drop ratio of strongly bound water was almost twice as high as that of weakly bound water, which meant that the relaxation times of strongly bound water and weakly bound water reflected the relaxation dynamics of coacervates at different time and length scales (Figure 3e). Unlike the dynamics of strongly bound water, which reflects the movement of polar groups on the protein side chains, the dynamics of weakly bound water in the gaps between protein molecules may reflect the disturbance of water by the overall movement of protein molecules in the coacervates. Interestingly, no free water was detected in coacervates with faster dynamics at the pH 6.0−6.8, while coacervates with slower dynamics at higher pH contained free water because it was difficult to expel free water introduced by structural inhomogeneity at large length scales through slow structural relaxation (Figure 3d).

3.3. Driving Force Analysis of Liquid, Gel, and Solid Coacervates

The physical properties and dynamics of coacervates are usually closely related to the driving forces of complex coacervation. Therefore, ITC was used to analyze the thermodynamics of the BLG-LYS complex coacervation at pH 6, 7, and 8. The integrated enthalpies at all three pH levels showed typical results of "one set of sites" and converged near the midpoint of the titration (Figure 4a−c). The stoichiometric ratios obtained by ITC were consistent with the results of the ζ-potential and supernatant protein content (Figure 4d). The apparent dissociation constant $K_{d,app}$ decreased significantly with increasing pH, indicating that the binding affinity between proteins increased with increasing pH, which can explain the liquid−gel−solid transition of coacervates and the corresponding slowed dynamics (Figure 4e).

However, the absolute value of ΔH decreased with an increase in pH, whereas entropy increased significantly (Figure 4f). This indicated that the increased binding affinity did not come from the enhanced electrostatic interaction but resulted from the entropy gains within the system, although the exotherm caused by electrostatic interaction was the main driving force for BLG-LYS complex coacervation at pH 6, 7, and 8. This result was consistent with the ionization degree of BLG and LYS. At pH 6, the carboxyl groups of BLG were almost completely ionized, whereas the N-terminal amino group of LYS and the imidazole group of His were

https://doi.org/10.1021/acs.biomac.6c00197
Biomacromolecules XXXX, XXX, XXX−XXX

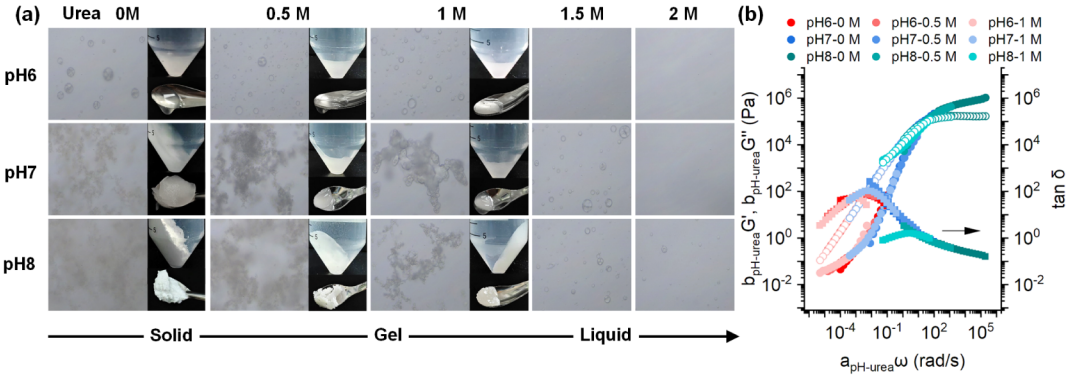

Figure 5. Bright-field microscopy images of BLG-LYS coacervates at pH 6, 7, and 8 containing 0−2 M urea (a). The time-pH-urea superposition of linear viscoelastic responses of BLG-LYS coacervates (b).

deprotonated as the pH increased from 6 to 8, which led to the weaker interaction between the oppositely charged patches (Figure S1a,b).

Complex coacervation causes a portion of the water molecules bound to proteins to be released into the dilute phase, causing an increase in entropy. The protein molecules and the water remaining in the coacervates reduce their degrees of freedom due to the dense, crowding environment, resulting in entropy loss.[81] Their tug-of-war determines the entropy change of the entire process. With the increase of pH, the entropy increase released by water molecules gradually overcame the entropy loss and won the thermodynamic advantage, resulting in the reversal of unfavorable entropy to favorable entropy. Therefore, the liquid−gel−solid transition and the slowdown of coacervation dynamics may be related to the entropic force of desolvation.

The content of bound water in BLG-LYS coacervates was evaluated to validate the desolvation effect. The total water content obtained by the TGA method and the proportion of water in each dynamics state obtained by spin−spin relaxation were combined to obtain the absolute content changes of various types of water in the coacervates (Figure 4g−i). The total water content of coacervates decreased with increasing pH from 6.0 to 7.5, and only increased at pH 8.0, consistent with the decreased G' and G'' at pH 8.0 (Figures 4g and 3a). The water content of the liquid coacervate at pH 6 was 60.21%, which meant that even the liquid BLG-LYS coacervate had a protein content of nearly 40% (Figure 4g). The content of strongly bound water in the coacervate decreased significantly with increasing pH. It decreased to only 0.1% at pH 7.5 and was even undetectable at pH 8.0. Similarly, the content of weakly bound water also decreased as the pH increased from 6.0 to 7.5. The abnormal increase in weakly bound water at pH 8.0 may be related to the measured high total water content because long length-scale structural inhomogeneity of the coacervate at pH 8 caused a large amount of free water to be doped inside and on the surface of the coacervate sample, which was observed during the sample preparation and was also confirmed by the significantly increased free water content (Figures 4i and 2a).

The loss of a large amount of bound water meant that the protein−water hydrogen bonds were converted into protein−protein hydrogen bonds, especially the complete loss of strongly bound water, which meant that polar groups on the protein surface almost all form protein−protein hydrogen bonds. During the pH-induced liquid−gel−solid transition, although long-range electrostatic interactions weaken with increasing pH, the number of short-range protein−protein hydrogen bonds increases, which can also lead to an increase in protein−protein binding affinity, resulting in a slowdown of coacervate dynamics.

3.4. Role of Hydrogen Bonding and Desolvation Effect

The amide A in infrared spectroscopy is key for studying protein−protein interactions.[82] When the N−H group acts as a hydrogen bond donor, it is partially "attracted" by the lone pair of electrons of the hydrogen acceptor. This interaction causes the electron density of the N−H bond to decrease, lowering the vibration frequency of the N−H bond and resulting in a redshift.[83] Protein−protein hydrogen bonds induce a greater bond extension and thus a larger redshift than protein−water bonds.[82] The FT-IR spectra of BLG, LYS, and the BLG-LYS coacervates at pH 6, 7, and 8 are shown in Figure S4. Compared to the individual BLG and LYS, the amide A band of the BLG-LYS coacervates exhibited a larger redshift, indicating the formation of protein−protein hydrogen bonds after phase separation. Moreover, the degree of redshift in the amide A band shows an increasing trend with an increase in pH in coacervates, suggesting an increase in hydrogen bond transfer.

The strong competition of urea for protein hydrogen bonds was used to study the effects of intermolecular hydrogen bonds on the physical properties, dynamics, and phase transitions of the BLG-LYS coacervates. Increasing urea concentration from 0 to 1.5 M induced a solid−gel−liquid transition (Figure 5a). Coacervate formation was completely inhibited at 2 M urea, which was much lower than those typically causing partial (4 M) or complete (6−8 M) protein denaturation.[84,85] This demonstrates that H-bonding is not only crucial for the pH-induced liquid−gel−solid transitions but is also a necessary driving force for coacervate formation itself. Furthermore, the urea concentration required to completely inhibit coacervation increased with pH, indicating that more intermolecular hydrogen bonds form at higher pH (Figure 5a). In addition, linear viscoelastic analysis showed that urea significantly reduced the G' and G'' of the coacervates and accelerated their dynamics. Time-pH-urea superposition was largely achievable (except for pH 8 with 1 M urea at low frequencies), confirming that hydrogen bonds critically regulate the dynamics of BLG-LYS coacervates (Figures 5b and S3h,i). The corresponding $a_{pH\text{-}urea}$ and $b_{pH\text{-}urea}$ values were presented in Figure S3d,e.

https://doi.org/10.1021/acs.biomac.6c00197
Biomacromolecules XXXX, XXX, XXX−XXX

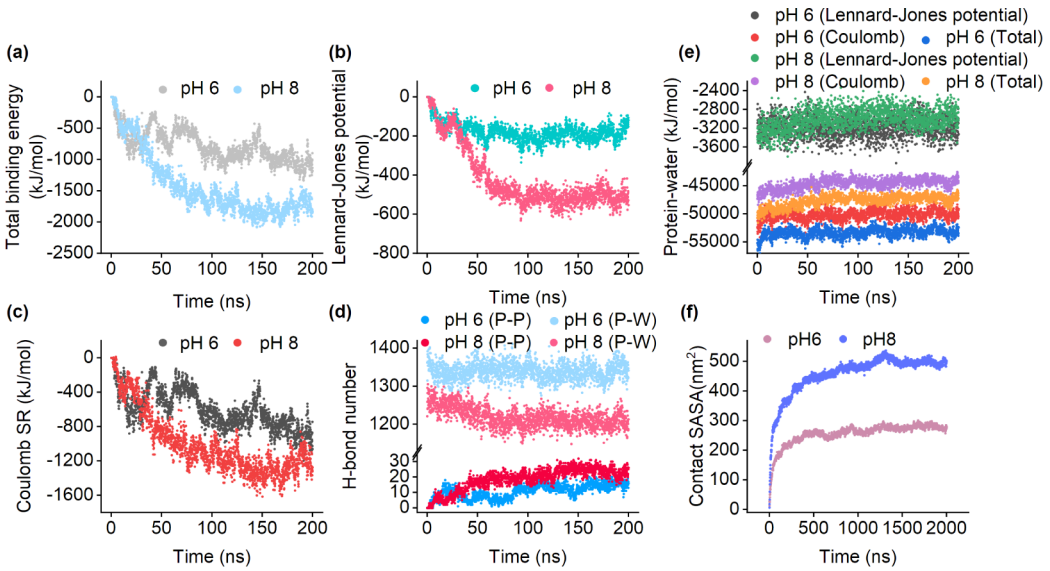

Figure 6. Total binding energy (a), Lennard-Jones potential (b), Coulomb SR (c), and H-bond number (d) of BLG-LYS interactions and the energy of protein−water interactions (e) at pH 6 and 8, obtained from all-atom MD simulations. Ratio of SASA between pH 8 and pH 6 systems over 0−2000 ns in coarse-grained simulations (f).

All-atom MD simulation (200 ns) was performed to verify the protein interactions and desolvation effect of the BLG-LYS complex coacervation. Each box contained four proteins (BLG:LYS = 3:1 at pH 6, BLG:LYS = 1:1 at pH 8), which was close to the SAXS-derived basic units. The Lennard-Jones potential, short-range Coulomb potential, and total binding energy between BLG and LYS during the complex coacervation at pH 8 were higher than those at pH 6 (Figure 6a−e). Specifically, the Lennard-Jones potential at pH 8 was 2.7 times greater than at pH 6 during the time intervals of 150−200 s, indicating more interaction interfaces at pH 8 (Figure 6b). As shown in Figure 7a, when BLG:LYS = 1:1, the interaction interface between BLG and LYS was more than that when BLG:LYS = 3:1. Considering that the all-atom MD simulation was limited by the total number of proteins, we used coarse-grained simulations to further verify the interaction interface area between BLG and LYS at two stoichiometries on a larger scale, which was obtained by solvent-accessible surface calculation. Coarse-grained simulation systems were built at pH 6 and 8 with protein ratios of 15:5 and 10:10, respectively, and SASA calculations indicated that the interaction interface at pH 8 formed more contacts, approximately 1.7 times greater than at pH 6 (Figure 6f). Furthermore, the absolute value of the binding energy between proteins and water molecules decreased significantly over time, with lower values at pH 8 compared to those at pH 6 (Figure 6a). In addition, the reduction in binding energy was mainly due to the decreased short-range Coulomb potential (i.e., hydrogen bond), which demonstrated significant desolvation. The degree of desolvation was higher at pH 8 (Figure 6a−c). This finding was also confirmed by tracking the dynamic changes in protein−water and protein−protein hydrogen bonds during complex coacervation (Figure 6d). Within 0−200 ns, BLG-LYS hydrogen bonds increased from 0 to 16 at pH 6 and to 26 at pH 8. The number of protein−water hydrogen bonds also decreased more at pH 8. The number of protein−water hydrogen bonds at pH 8 was 1.625 times that at pH 6, consistent with the SASA results, further confirming the

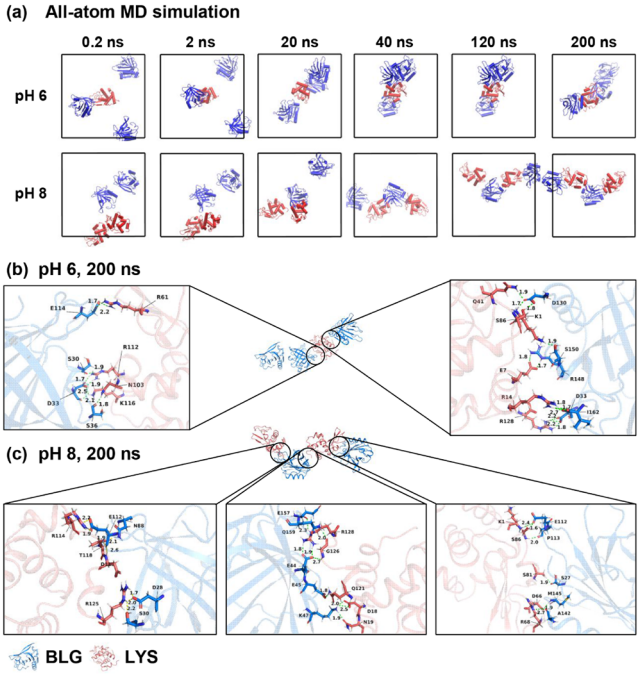

Figure 7. Snapshots of the coacervate unit formed by BLG and LYS during all-atom molecular dynamics simulations (a). Interaction sites of BLG and LYS in all-atom molecular dynamics simulations at 200 ns at pH 6 (b) and 8 (c).

enhanced desolvation and stronger protein−protein interactions at higher pH.

Finally, the interaction sites at 200 ns were analyzed. The main groups involved in the formation of hydrogen bonds were amino acids with charged side chains, such as arginine and lysine in LYS as well as aspartic acid and glutamic acid in BLG, showing that long-range electrostatic interactions were closely related to the formation of hydrogen bonds (Figures 7a,b and S5). In addition, the side chain amide groups (asparagine and glutamine) and hydroxyl groups of polar amino acids were also involved in forming BLG-LYS hydrogen bonds. In addition to

https://doi.org/10.1021/acs.biomac.6c00197
Biomacromolecules XXXX, XXX, XXX−XXX

the above groups, amide groups of hydrophobic amino acids such as glycine, proline, and methionine also formed interprotein hydrogen bonds at pH 8, which may be related to the higher desolvation degree at pH 8. The desolvation environment in the coacervate also promoted the generation of hydrophobic interactions in the coacervate. Altogether, these results pointed to the fact that pH-induced stoichiometric changes affected hydrogen bonding, desolvation, dynamics, and matter state in a stepwise manner by affecting the number of heteroprotein (BLG-LYS) interaction interfaces within the coacervates.

4. CONCLUSIONS AND FUTURE PERSPECTIVES

This study reported the liquid−gel−solid transition of food protein coacervates composed of BLG and LYS as the charge symmetry increased. Experimental techniques, including SAXS, rheology, calorimetry, and LF-NMR, combined with all-atom MD simulations, provided detailed insights into the dynamics and thermodynamic mechanisms underlying the physical properties of coacervates composed of globular food proteins. The liquid−gel−solid transition of BLG-LYS coacervates was demonstrated by the slowed dynamics of water and the time-pH superposition of the linear viscoelastic responses. The power law for the shift factor a_{pH} demonstrated a strong linear relationship with pH, showing that a one-unit increase in pH slowed the terminal relaxation time of the coacervate by 3.4 orders of magnitude. Despite a decrease in long-range electrostatic interactions during this transition, the change in pH-driven charge variation of BLG and LYS caused the stoichiometric ratio (BLG/LYS) of the coacervate to shift gradually from 3:1 to 1:1. And all-atom molecular dynamics simulations revealed that this shift in the stoichiometric ratio increased charge symmetry, increasing the number of interaction interfaces between BLG and LYS. The long-range electrostatic interaction at the BLG-LYS interface promoted intermolecular hydrogen bond formation and the desolvation of bound water, strengthening the binding energy between the proteins and driving the liquid−gel−solid transition of the coacervate. Food protein coacervates are a type of highly crowded soft matter distinct from typical protein solutions, with promising applications in developing innovative food systems based on proteins. Although many disciplines have conducted long-term research on the coacervation of synthetic polyelectrolytes and disordered biomolecules, the theoretical understanding of the coacervation composed solely of globular proteins and their physical states remains limited. Our understanding of the physical property transition caused by the stoichiometric ratio and charge symmetry of protein coacervates is likely to be transferable to synthetic polyelectrolytes and biomolecular condensates, providing a new perspective for multidisciplinary exploration of the physical property and functional changes in coacervate materials.

■ ASSOCIATED CONTENT

Supporting Information

The Supporting Information is available free of charge at https://pubs.acs.org/doi/10.1021/acs.biomac.6c00197.

All-Atom Molecular Dynamics Simulation of the Interaction between Three BLG Molecules and One LYS Molecule at pH 6.0 (MP4)

All-Atom Molecular Dynamics Simulation of the Interaction between Two BLG Molecules and Two LYS Molecules at pH 8.0 (MP4)

Coarse-Grained Molecular Dynamics Simulation of the Multiscale Assembly between 15 BLG and 5 LYS Molecules at pH 6.0 (MP4)

Coarse-Grained Molecular Dynamics Simulation of the Multiscale Assembly between 10 BLG and 10 LYS Molecules at pH 8.0 (MP4)

Figure S1: Ionization curves of charged amino acids in BLG (a) and LYS (b) at pH 2−12. Estimated net charge (c) and ζ-potential (d) of BLG and LYS at pH 5−9; Figure S2: Effects of pH and mixing ratio on turbidity (a), protein recovery ratio (b), and ζ-potential (c) of BLG-LYS systems, as well as the obtained stoichiometric ratios (d) of the BLG-LYS complex; Figure S3: Amplitude sweeps (0.01−1% strain at 100 rad/s) for the BLG-LYS coacervates at pH 5.5−9.0 (a). Amplitude sweeps (0.01−1% strain at 100 rad/s) for the BLG-LYS coacervates containing 0−1 M urea (b). Vertical shift factors (b_{pH}) for the BLG-LYS coacervates (c). Horizontal shift factors ($a_{pH\text{-}urea}$) (d) and vertical shift factors ($b_{pH\text{-}urea}$) (e) for the BLG-LYS coacervates with the addition of urea. Cole−Cole plots (f) and van Gurp−Palmen plots (g) for the BLG-LYS coacervates. Cole−Cole plots (h) and van Gurp−Palmen plots (i) for the BLG-LYS coacervates containing urea; Figure S4: The FTIR spectra of BLG, LYS, and BLG-LYS coacervates at pH 6, 7, and 8; Figure S5: Interaction sites of BLG and LYS in all-atom molecular dynamics simulations at 200 ns at pH 6 and 8, obtained from LigPlot; Figure S6: Plots of (a) tan δ, (b) the normalized phase angle ($2\delta/\pi$), (c) the normalized elastic modulus (G'/G^*), and (d) the normalized viscous modulus (G''/G^*) as a function of the pH. Data are shown for frequencies ranging from 1 rad/s to 100 rad/s (purple to red), also indicated by the arrows. The gel point is extrapolated to occur at a pH greater than 8.0, based on the trajectory of the frequency-invariant crossover point observed in all figures (PDF)

■ AUTHOR INFORMATION

Corresponding Authors

Jiabao Zheng − *School of Food Science and Engineering, South China University of Technology, Guangzhou 510641, PR China*; Email: jiabaozheng@scut.edu.cn

Weizheng Sun − *School of Food Science and Engineering, South China University of Technology, Guangzhou 510641, PR China*; orcid.org/0000-0001-5769-4275; Email: fewzhsun@scut.edu.cn

Authors

Jiaxuan Zhang − *School of Food Science and Engineering, South China University of Technology, Guangzhou 510641, PR China*; orcid.org/0009-0004-0413-1435

Jiajia Zhou − *School of Emergent Soft Matter, South China University of Technology, Guangzhou 510641, PR China*; orcid.org/0000-0002-2258-6757

Fei Pan − *State Key Laboratory of Resource Insects, Institute of Apicultural Research, Chinese Academy of Agricultural Sciences, Beijing 100093, China*

Complete contact information is available at:

https://doi.org/10.1021/acs.biomac.6c00197
Biomacromolecules XXXX, XXX, XXX−XXX

https://pubs.acs.org/10.1021/acs.biomac.6c00197

Author Contributions

W.S. and Jb.Z. led and supervised the project. Jx.Z. performed the experiments. Jb.Z., Jx.Z., and Jj.Z. undertook the data analysis, wrote the manuscript, discussed the results, and have given approval to the final version of the manuscript.

Notes

The authors declare no competing financial interest.

■ ACKNOWLEDGMENTS

This work was supported by the National Key Research and Development Program of China (2024YFF1106503), the National Natural Science Foundation of China (22478132; 32402178), Science and Technology Projects in Guangzhou (2024B03J1314), and the Guangdong Basic and Applied Basic Research Foundation (2024A1515012638; 2023A1515110600).

■ REFERENCES

(1) Brangwynne, C. P.; Mitchison, T. J.; Hyman, A. A. Active liquid-like behavior of nucleoli determines their size and shape in Xenopus laevis oocytes. *Proc. Natl. Acad. Sci. U. S. A* **2011**, *108* (11), 4334−4339.

(2) Banani, S. F.; Lee, H. O.; Hyman, A. A.; Rosen, M. K. Biomolecular condensates: organizers of cellular biochemistry. *Nat. Rev. Mol. Cell Biol* **2017**, *18* (5), 285−298.

(3) Alberti, S.; Gladfelter, A.; Mittag, T. Considerations and challenges in studying liquid-liquid phase separation and biomolecular condensates. *Cell* **2019**, *176* (3), 419−434.

(4) Abyzov, A.; Blackledge, M.; Zweckstetter, M. Conformational Dynamics of Intrinsically Disordered Proteins Regulate Biomolecular Condensate Chemistry. *Chem. Rev* **2022**, *122* (6), 6719−6748.

(5) Boire, A.; Renard, D.; Bouchoux, A.; Pezennec, S.; Croguennec, T.; Lechevalier, V.; Le Floch-Fouere, C.; Bouhallab, S.; Menut, P. Soft-matter approaches for controlling food protein interactions and assembly. *Annu. Rev. Food Sci. Technol* **2019**, *10*, 521−539.

(6) Zheng, J.; Tang, C.-H.; Ge, G.; Zhao, M.; Sun, W. Heteroprotein complex of soy protein isolate and lysozyme: Formation mechanism and thermodynamic characterization. *Food Hydrocolloids* **2020**, *101*, 105571.

(7) Croguennec, T.; Tavares, G. M.; Bouhallab, S. Heteroprotein complex coacervation: A generic process. *Adv. Colloid Interface Sci* **2017**, *239*, 115−126.

(8) Zheng, J.; Gao, Q.; Ge, G.; Wu, J.; Tang, C.-H.; Zhao, M.; Sun, W. Dynamic equilibrium of β-conglycinin/lysozyme heteroprotein complex coacervates. *Food Hydrocolloids* **2022**, *124*, 107339.

(9) Zheng, J.; Gao, Q.; Ge, G.; Wu, J.; Tang, C.-H.; Zhao, M.; Sun, W. Heteroprotein Complex Coacervate Based on β-Conglycinin and Lysozyme: Dynamic Protein Exchange, Thermodynamic Mechanism, and Lysozyme Activity. *J. Agric. Food Chem* **2021**, *69* (28), 7948−7959.

(10) Tavares, G. M.; Croguennec, T.; Hamon, P.; Carvalho, A. F.; Bouhallab, S. Selective coacervation between lactoferrin and the two isoforms of β-lactoglobulin. *Food Hydrocolloids* **2015**, *48*, 238−247.

(11) Soussi Hachfi, R.; Famelart, M.-H.; Rousseau, F.; Hamon, P.; Bouhallab, S. Rheological characterization of β-lactoglobulin/Lactoferrin complex coacervates. *LWT* **2022**, *163*, 113577.

(12) Yan, Y.; Kizilay, E.; Seeman, D.; Flanagan, S.; Dubin, P. L.; Bovetto, L.; Donato, L.; Schmitt, C. Heteroprotein complex coacervation: bovine β-lactoglobulin and lactoferrin. *Langmuir* **2013**, *29* (50), 15614−15623.

(13) Peixoto, P. D. S.; Tavares, G. M.; Croguennec, T.; Nicolas, A.; Hamon, P.; Roiland, C.; Bouhallab, S. Structure and Dynamics of Heteroprotein Coacervates. *Langmuir* **2016**, *32* (31), 7821−7828.

(14) Kizilay, E.; Seeman, D.; Yan, Y.; Du, X.; Dubin, P. L.; Donato-Capel, L.; Bovetto, L.; Schmitt, C. Structure of bovine β-lactoglobulin−lactoferrin coacervates. *Soft Matter* **2014**, *10* (37), 7262−7268.

(15) Flanagan, S. E.; Malanowski, A. J.; Kizilay, E.; Seeman, D.; Dubin, P. L.; Donato-Capel, L.; Bovetto, L.; Schmitt, C. Complex Equilibria, Speciation, and Heteroprotein Coacervation of Lactoferrin and β-Lactoglobulin. *Langmuir* **2015**, *31* (5), 1776−1783.

(16) Adal, E.; Sadeghpour, A.; Connell, S.; Rappolt, M.; Ibanoglu, E.; Sarkar, A. Heteroprotein complex formation of bovine lactoferrin and pea protein isolate: a multiscale structural analysis. *Biomacromolecules* **2017**, *18* (2), 625−635.

(17) Bungenberg de Jong, H. G.; Kruyt, H. R. Coacervation (partial miscibility in colloid systems). *Proc. K. Ned. Akad. Wet* **1929**, *32*, 849−856.

(18) Mitrea, D. M.; Mittasch, M.; Gomes, B. F.; Klein, I. A.; Murcko, M. A. Modulating biomolecular condensates: a novel approach to drug discovery. *Nat. Rev. Drug Discovery* **2022**, *21* (11), 841−862.

(19) Brangwynne, C. P.; Eckmann, C. R.; Courson, D. S.; Rybarska, A.; Hoege, C.; Gharakhani, J.; Jülicher, F.; Hyman, A. A. Germline P Granules Are Liquid Droplets That Localize by Controlled Dissolution/Condensation. *Science* **2009**, *324* (5935), 1729−1732.

(20) Patel, A.; Lee, H. O.; Jawerth, L.; Maharana, S.; Jahnel, M.; Hein, M. Y.; Stoynov, S.; Mahamid, J.; Saha, S.; Franzmann, T. M.; Pozniakovski, A.; Poser, I.; Maghelli, N.; Royer, L. A.; Weigert, M.; Myers, E. W.; Grill, S.; Drechsel, D.; Hyman, A. A.; Alberti, S. A Liquid-to-Solid Phase Transition of the ALS Protein FUS Accelerated by Disease Mutation. *Cell* **2015**, *162* (5), 1066−1077.

(21) Molliex, A.; Temirov, J.; Lee, J.; Coughlin, M.; Kanagaraj, A. P.; Kim, H. J.; Mittag, T.; Taylor, J. P. Phase Separation by Low Complexity Domains Promotes Stress Granule Assembly and Drives Pathological Fibrillization. *Cell* **2015**, *163* (1), 123−133.

(22) Woodruff, J. B.; Ferreira Gomes, B.; Widlund, P. O.; Mahamid, J.; Honigmann, A.; Hyman, A. A. The Centrosome Is a Selective Condensate that Nucleates Microtubules by Concentrating Tubulin. *Cell* **2017**, *169* (6), 1066−1077.e10.

(23) Jain, A.; Vale, R. D. RNA phase transitions in repeat expansion disorders. *Nature* **2017**, *546* (7657), 243−247.

(24) Frey, S.; Richter, R. P.; Görlich, D. FG-Rich Repeats of Nuclear Pore Proteins Form a Three-Dimensional Meshwork with Hydrogel-Like Properties. *Science* **2006**, *314* (5800), 815−817.

(25) Boke, E.; Ruer, M.; Wühr, M.; Coughlin, M.; Lemaitre, R.; Gygi, S. P.; Alberti, S.; Drechsel, D.; Hyman, A. A.; Mitchison, T. J. Amyloid-like Self-Assembly of a Cellular Compartment. *Cell* **2016**, *166* (3), 637−650.

(26) Audas, T. E.; Audas, D. E.; Jacob, M. D.; Ho, J. J. D.; Khacho, M.; Wang, M.; Perera, J. K.; Gardiner, C.; Bennett, C. A.; Head, T.; Kryvenko, O. N.; Jorda, M.; Daunert, S.; Malhotra, A.; Trinkle-Mulcahy, L.; Gonzalgo, M. L.; Lee, S. Adaptation to Stressors by Systemic Protein Amyloidogenesis. *Dev. Cell* **2016**, *39* (2), 155−168.

(27) Zheng, J.; Van der Meeren, P.; Sun, W. New insights into protein−polysaccharide complex coacervation: Dynamics, molecular parameters, and applications. *Aggregate* **2024**, *5* (1), No. e449.

(28) Perry, S. L.; Leon, L.; Hoffmann, K. Q.; Kade, M. J.; Priftis, D.; Black, K. A.; Wong, D.; Klein, R. A.; Pierce, C. F.; Margossian, K. O.; Whitmer, J. K.; Qin, J.; de Pablo, J. J.; Tirrell, M. Chirality-selected phase behaviour in ionic polypeptide complexes. *Nat. Commun* **2015**, *6* (1), 6052.

(29) Hoffmann, K. Q.; Perry, S. L.; Leon, L.; Priftis, D.; Tirrell, M.; de Pablo, J. J. A molecular view of the role of chirality in charge-driven polypeptide complexation. *Soft Matter* **2015**, *11* (8), 1525−1538.

(30) Pacalin, N. M.; Leon, L.; Tirrell, M. Directing the phase behavior of polyelectrolyte complexes using chiral patterned peptides. *Eur. Phys. J. Spec Top* **2016**, *225* (8), 1805−1815.

(31) Zervoudis, N. A.; Obermeyer, A. C. The effects of protein charge patterning on complex coacervation. *Soft Matter* **2021**, *17* (27), 6637−6645.

(32) Chang, L.-W.; Lytle, T. K.; Radhakrishna, M.; Madinya, J. J.; Vélez, J.; Sing, C. E.; Perry, S. L. Sequence and entropy-based control of complex coacervates. *Nat. Commun* **2017**, *8* (1), 1273.
(33) Lytle, T. K.; Chang, L.-W.; Markiewicz, N.; Perry, S. L.; Sing, C. E. Designing Electrostatic Interactions via Polyelectrolyte Monomer Sequence. *ACS Cent. Sci* **2019**, *5* (4), 709−718.
(34) Blocher McTigue, W. C.; Perry, S. L. Design rules for encapsulating proteins into complex coacervates. *Soft Matter* **2019**, *15* (15), 3089−3103.
(35) Samanta, R.; Ganesan, V. Influence of protein charge patches on the structure of protein-polyelectrolyte complexes. *Soft Matter* **2018**, *14* (46), 9475−9488.
(36) Samanta, R.; Halabe, A.; Ganesan, V. Influence of Charge Regulation and Charge Heterogeneity on Complexation between Polyelectrolytes and Proteins. *J. Phys. Chem. B* **2020**, *124* (22), 4421−4435.
(37) Es Sayed, J.; Caïto, C.; Arunachalam, A.; Amirsadeghi, A.; van Westerveld, L.; Maret, D.; Mohamed Yunus, R. A.; Calicchia, E.; Dittberner, O.; Portale, G.; Parisi, D.; Kamperman, M. Effect of Dynamically Arrested Domains on the Phase Behavior, Linear Viscoelasticity and Microstructure of Hyaluronic Acid − Chitosan Complex Coacervates. *Macromolecules* **2023**, *56* (15), 5891−5904.
(38) Ramírez Marrero, I. A.; Boudreau, L.; Hu, W.; Gutzler, R.; Kaiser, N.; von Vacano, B.; Konradi, R.; Perry, S. L. Decoupling the Effects of Charge Density and Hydrophobicity on the Phase Behavior and Viscoelasticity of Complex Coacervates. *Macromolecules* **2024**, *57* (10), 4680−4694.
(39) Huang, J.; Laaser, J. E. Charge Density and Hydrophobicity-Dominated Regimes in the Phase Behavior of Complex Coacervates. *ACS Macro Lett* **2021**, *10* (8), 1029−1034.
(40) Tabandeh, S.; Leon, L. Engineering Peptide-Based Polyelectrolyte Complexes with Increased Hydrophobicity. *Molecules* **2019**, *24*, 868.
(41) Sadman, K.; Wang, Q.; Chen, Y.; Keshavarz, B.; Jiang, Z.; Shull, K. R. Influence of Hydrophobicity on Polyelectrolyte Complexation. *Macromolecules* **2017**, *50* (23), 9417−9426.
(42) Sathyavageeswaran, A.; Pandey, P. K.; Holmlund, N.; Kaushik, P.; McIntosh, S.; Mokdad, R.; Perry, S. L. Role of Charge Patterning and Hydrophobicity in Peptide-Based Complex Coacervates. *Biomacromolecules* **2025**, *26* (10), 6574−6585.
(43) Kayitmazer, A. B.; Koksal, A. F.; Kilic Iyilik, E. Complex coacervation of hyaluronic acid and chitosan: effects of pH, ionic strength, charge density, chain length and the charge ratio. *Soft Matter* **2015**, *11* (44), 8605−8612.
(44) Spruijt, E.; Cohen Stuart, M. A.; van der Gucht, J. Linear viscoelasticity of polyelectrolyte complex coacervates. *Macromolecules* **2013**, *46* (4), 1633−1641.
(45) Liu, Y.; Santa Chalarca, C. F.; Carmean, R. N.; Olson, R. A.; Madinya, J.; Sumerlin, B. S.; Sing, C. E.; Emrick, T.; Perry, S. L. Effect of polymer chemistry on the linear viscoelasticity of complex coacervates. *Macromolecules* **2020**, *53* (18), 7851−7864.
(46) Akkaoui, K.; Yang, M.; Digby, Z. A.; Schlenoff, J. B. Ultraviscosity in Entangled Polyelectrolyte Complexes and Coacervates. *Macromolecules* **2020**, *53* (11), 4234−4246.
(47) Yang, M.; Shi, J.; Schlenoff, J. B. Control of dynamics in polyelectrolyte complexes by temperature and salt. *Macromolecules* **2019**, *52* (5), 1930−1941.
(48) Wang, Q.; Schlenoff, J. B. The Polyelectrolyte Complex/Coacervate Continuum. *Macromolecules* **2014**, *47* (9), 3108−3116.
(49) Perry, S. L.; Li, Y.; Priftis, D.; Leon, L.; Tirrell, M. The Effect of Salt on the Complex Coacervation of Vinyl Polyelectrolytes. *Polymers* **2014**, *6*, 1756−1772.
(50) Li, L.; Srivastava, S.; Andreev, M.; Marciel, A. B.; de Pablo, J. J.; Tirrell, M. V. Phase Behavior and Salt Partitioning in Polyelectrolyte Complex Coacervates. *Macromolecules* **2018**, *51* (8), 2988−2995.
(51) Schröder, P.; Schönhoff, M.; Cramer, C. Validity and Breakdown of Superposition Principles in the Viscoelasticity of Chitosan−Gum Arabic Complex Coacervates. *Macromolecules* **2023**, *56* (13), 4966−4980.
(52) Ali, S.; Bleuel, M.; Prabhu, V. M. Lower Critical Solution Temperature in Polyelectrolyte Complex Coacervates. *ACS Macro Lett* **2019**, *8* (3), 289−293.
(53) Ma, Y.; Prabhu, V. M. Cosolvent Control of Lower and Upper Critical Solution Behavior in Polyelectrolyte Complexes. *ACS Macro Lett* **2025**, *14* (7), 962−968.
(54) Lalwani, S. M.; Batys, P.; Sammalkorpi, M.; Lutkenhaus, J. L. Relaxation Times of Solid-like Polyelectrolyte Complexes of Varying pH and Water Content. *Macromolecules* **2021**, *54* (17), 7765−7776.
(55) Tekaat, M.; Bütergerds, D.; Schönhoff, M.; Fery, A.; Cramer, C. Scaling properties of the shear modulus of polyelectrolyte complex coacervates: a time-pH superposition principle. *Phys. Chem. Chem. Phys* **2015**, *17* (35), 22552−22556.
(56) Khoonkari, M.; Es Sayed, J.; Oggioni, M.; Amirsadeghi, A.; Dijkstra, P.; Parisi, D.; Kruyt, F.; van Rijn, P.; Włodarczyk-Biegun, M. K.; Kamperman, M. Bioinspired Processing: Complex Coacervates as Versatile Inks for 3D Bioprinting. *Adv. Mater* **2023**, *35* (28), 2210769.
(57) Meng, X.; Schiffman, J. D.; Perry, S. L. Electrospinning cargo-containing polyelectrolyte complex fibers: correlating molecular interactions to complex coacervate phase behavior and fiber formation. *Macromolecules* **2018**, *51* (21), 8821−8832.
(58) Meng, X.; Du, Y.; Liu, Y.; Coughlin, E. B.; Perry, S. L.; Schiffman, J. D. Electrospinning Fibers from Oligomeric Complex Coacervates: No Chain Entanglements Needed. *Macromolecules* **2021**, *54* (11), 5033−5042.
(59) Sun, J.; Perry, S. L.; Schiffman, J. D. Electrospinning Nanofibers from Chitosan/Hyaluronic Acid Complex Coacervates. *Biomacromolecules* **2019**, *20* (11), 4191−4198.
(60) Kolibaba, T. J.; Higgins, C. I.; Crawford, N. C.; Samaniuk, J. R.; Killgore, J. P. Sustainable Additive Manufacturing of Polyelectrolyte Photopolymer Complexes. *Adv Mater. Technol.* **2023**, *8* (9), 2201681.
(61) Kolibaba, T. J.; Caplins, B. W.; Higgins, C. I.; Mansfield, E.; Miller, S. L.; Chandler, C.; Killgore, J. P. Tailoring Properties of 3D-Printable Polyelectrolyte Photopolymer Complexes with Reactive Diluents. *ACS Appl. Polym. Mater* **2024**, *6* (12), 6957−6965.
(62) Zhu, F.; Cheng, L.; Yin, J.; Wu, Z. L.; Qian, J.; Fu, J.; Zheng, Q. 3D Printing of Ultratough Polyion Complex Hydrogels. *ACS Appl. Mater. Interfaces* **2016**, *8* (45), 31304−31310.
(63) Spoelstra, W. K.; van der Sluis, E. O.; Dogterom, M.; Reese, L. Nonspherical coacervate shapes in an enzyme-driven active system. *Langmuir* **2020**, *36* (8), 1956−1964.
(64) Gao, N.; Mann, S. Membranized Coacervate Microdroplets: from Versatile Protocell Models to Cytomimetic Materials. *Acc. Chem. Res* **2023**, *56* (3), 297−307.
(65) Brangwynne, C. P.; Tompa, P.; Pappu, R. V. Polymer physics of intracellular phase transitions. *Nat. Phys* **2015**, *11* (11), 899−904.
(66) Wu, T.; Jiang, Q.; Wu, D.; Hu, Y.; Chen, S.; Ding, T.; Ye, X.; Liu, D.; Chen, J. What is new in lysozyme research and its application in food industry? A review. *Food Chem* **2019**, *274*, 698−709.
(67) Johansson, M. U.; Zoete, V.; Michielin, O.; Guex, N. Defining and searching for structural motifs using DeepView/Swiss-PdbViewer. *BMC Bioinf* **2012**, *13* (1), 173.
(68) Anandakrishnan, R.; Aguilar, B.; Onufriev, A. V. H++ 3.0: automating pK prediction and the preparation of biomolecular structures for atomistic molecular modeling and simulations. *Nucleic Acids Res* **2012**, *40* (W1), W537−W541.
(69) Abraham, M. J.; Murtola, T.; Schulz, R.; Páll, S.; Smith, J. C.; Hess, B.; Lindahl, E. GROMACS: High performance molecular simulations through multi-level parallelism from laptops to supercomputers. *SoftwareX* **2015**, *1−2*, 19−25.
(70) Gorelov, S.; Titov, A.; Tolicheva, O.; Konevega, A.; Shvetsov, A. DSSP in GROMACS: Tool for Defining Secondary Structures of Proteins in Trajectories. *J. Chem. Inf. Model* **2024**, *64* (9), 3593−3598.
(71) Xu, A. Y.; Melton, L. D.; Ryan, T. M.; Mata, J. P.; Rekas, A.; Williams, M. A. K.; McGillivray, D. J. Effects of polysaccharide charge pattern on the microstructures of β-lactoglobulin-pectin complex coacervates, studied by SAXS and SANS. *Food Hydrocolloids* **2018**, *77*, 952−963.

https://doi.org/10.1021/acs.biomac.6c00197
Biomacromolecules XXXX, XXX, XXX−XXX

(72) Zhang, X.; Zhang, Z.; Zhang, T.; Zhang, Y.; Jiang, L.; Sui, X. Heteroprotein complex coacervates of soy protein isolate and type-A gelatin: Formation mechanism, structure and rheological properties. *Food Hydrocolloids* **2025**, *158*, 110533.
(73) Roessle, M.; Svergun, D. I. *Small Angle X-ray Scattering*. Springer: Berlin, Heidelberg, 2013.
(74) Banks, A.; Qin, S.; Weiss, K. L.; Stanley, C. B.; Zhou, H.-X. Intrinsically Disordered Protein Exhibits Both Compaction and Expansion under Macromolecular Crowding. *Biophys. J* **2018**, *114* (5), 1067−1079.
(75) Hou, S.; Hu, J.; Yu, Z.; Li, D.; Liu, C.; Zhang, Y. Machine learning predictor PSPire screens for phase-separating proteins lacking intrinsically disordered regions. *Nat. Commun* **2024**, *15* (1), 2147.
(76) Liu, Y.; Winter, H. H.; Perry, S. L. Linear viscoelasticity of complex coacervates. *Adv. Colloid Interface Sci* **2017**, *239*, 46−60.
(77) Liu, Y.; Momani, B.; Winter, H. H.; Perry, S. L. Rheological characterization of liquid-to-solid transitions in bulk polyelectrolyte complexes. *Soft Matter* **2017**, *13* (40), 7332−7340.
(78) Larson, R. G.; Liu, Y.; Li, H. Linear viscoelasticity and time-temperature-salt and other superpositions in polyelectrolyte coacervates. *J. Rheol* **2021**, *65* (1), 77−102.
(79) Tang, S.; Wang, M.; Olsen, B. D. Anomalous Self-Diffusion and Sticky Rouse Dynamics in Associative Protein Hydrogels. *J. Am. Chem. Soc* **2015**, *137* (11), 3946−3957.
(80) Marciel, A. B.; Srivastava, S.; Tirrell, M. V. Structure and rheology of polyelectrolyte complex coacervates. *Soft Matter* **2018**, *14* (13), 2454−2464.
(81) Mukherjee, S.; Schäfer, L. V. Thermodynamic forces from protein and water govern condensate formation of an intrinsically disordered protein domain. *Nat. Commun* **2023**, *14* (1), 5892.
(82) Barth, A.; Zscherp, C. What vibrations tell about proteins. *Q. Rev. Biophys* **2002**, *35* (4), 369−430.
(83) Kong, J.; Yu, S. Fourier Transform Infrared Spectroscopic Analysis of Protein Secondary Structures. *Acta Biochim. Biophys. Sin* **2007**, *39* (8), 549−559.
(84) Timasheff, S. N.; Xie, G. Preferential interactions of urea with lysozyme and their linkage to protein denaturation. *Biophys. Chem* **2003**, *105* (2), 421−448.
(85) Canchi, D. R.; Paschek, D.; García, A. E. Equilibrium Study of Protein Denaturation by Urea. *J. Am. Chem. Soc* **2010**, *132* (7), 2338−2344.

https://doi.org/10.1021/acs.biomac.6c00197
Biomacromolecules XXXX, XXX, XXX−XXX